

1 **Study on the influence of topography on wind shear-**
2 **numerical simulation based on WRF-CALMET**

3 Xingyu Wang¹, Yuhong Lei¹, Baolong Shi¹, Zhiyi Wang¹, Xu Li¹, Jinyan Wang¹

4 ¹Key Laboratory of Climate Resource Development and Disaster Prevention in
5 Gansu Province, College of Atmospheric Sciences, Lanzhou University, Lanzhou
6 730000, China

7 **Correspondence:** Jinyan Wang (wangjny@lzu.edu.cn)

8 **Abstract**

9 This study focuses on the critical issue of low-altitude wind shear, vital for
10 aircraft safety during takeoff and landing. Using the WRF-CALMET model, we assess
11 the impact of topography on low-level wind shear at Zhongchuan Airport. CALMET
12 outperforms WRF, showing improved simulation accuracy. CALMET's simulation
13 highlights diurnal variations in vertical wind shear, especially pronounced from
14 13:00 to 24:00. Notably, CALMET indicates 1-2 hazard levels higher wind shear for
15 aircraft operations compared to WRF in a significant area. Terrain sensitivity
16 experiments reveal CALMET's responsiveness to terrain changes during high wind
17 shear periods, with reduced impact at higher altitudes. CALMET's incorporation of
18 kinematic terrain influences, blocking effects, slope flow, and strengthened diversion
19 of near-surface airflow on complex terrain contribute to these findings. This study
20 confirms the efficacy of CALMET in simulating low-altitude wind shear, emphasizing
21 its superiority in capturing terrain influences and reducing the aviation safety threat
22 posed by low-altitude wind shear.

23 **Keywords** — wind shear; wind field-numerical simulation; airport; CALMET;
24 aeronautical meteorology; topographic effect

25 **1. Introduction**

26 According to the definition of the International Civil Aviation Organization
27 (ICAO), low-level windshear refers to the sharp change of spatial wind speed or
28 direction within a 600-meter altitude range. Wind shear includes both vertical and
29 horizontal components and typically occurs near fronts, coastlines and the surface. In
30 the process of taking off and landing, low-level wind shear will affect the airspeed of
31 the aircraft, causing great risks and even terrible accidents in serious cases (Evans
32 J, 1989). In June 1975, a Boeing 727 aircraft crashed during its landing at Kennedy
33 Airport due to encountering low-level wind shear, resulting in 113 fatalities and 11
34 injuries (Fujita T T, 1997); In June 2000, a Wuhan Airlines aircraft crashed during
35 landing, also due to encountering low-level wind shear. In 2017, a New Zealand

36 Airlines A320-200 aircraft experienced low-level wind shear during landing,
37 resulting in severe damage to the aircraft and significant economic losses. Therefore,
38 accurate simulation and prediction of low-level wind shear, especially on complex
39 terrain, is of great significance for ensuring the safety of aircraft takeoffs and landings
40 at airports.

41 However, achieving accurate predictions remains a primary challenge faced by
42 numerical weather forecasting models (Colman B.2012). Low-level wind shear is
43 influenced by multiscale weather systems and characterized by small temporal and
44 spatial scales, high intensity, and sudden occurrences, thus making it difficult to
45 detect, study and predict. In simulating actual wind fields, simple characteristics are
46 insufficient; the wind field structure around the airport must be included. There are
47 three main methods for calculating wind shear in model wind fields(Zhang
48 Y,2022):1.Using meteorological radar networks and various monitoring networks
49 around airports, differential methods are employed to collect measured data,
50 recording wind speed, and wind direction in a grid format. However, these
51 measurements are scattered and small, insufficient to capture the essential
52 characteristics and dynamic development of low-level wind shear, and do not vary
53 with meteorological conditions.2.The second type of wind shear model is common in
54 engineering and consists of simple models. These typically comprise some physical
55 concepts, represented through simple mathematical fitting and basic fluid dynamics
56 solutions. They only reflect essential features of the shear wind field without fully
57 capturing the true wind field characteristics(Li Hai,2016).3.The third type of wind
58 shear model is based on atmospheric dynamics and physical equations, solved
59 directly by large computers. Among these methods, the third not only simulates the
60 real wind shear in the wind field but also provides other useful physical quantities
61 (e.g., temperature, water content, and radar reflectivity), revealing the formation
62 process, causes, and development of wind shear. Many studies have utilized
63 numerical models to simulate low-level wind shear.

64 Boilley used the non-hydrostatic Meso-NH model to simulate two different wind
65 shear events in the complex terrain around Nice Côte d'Azur Airport. They
66 successfully predicted vertical wind shear and local turbulence; however, due to the
67 model resolution limitation (500m), the study did not accurately predict the time and
68 location of low-level wind shear. Consequently, subsequent wind shear studies have
69 continuously improved spatial resolution. The Weather Research and Forecasting
70 (WRF) model, designed for high-resolution mesoscale weather forecasting, simulates
71 airflow under realistic atmospheric conditions. However, due to the grid resolution
72 of WRF being greater than 1 km, it struggles to simulate the small-scale airflow
73 movements in complex terrain.Hong Kong International Airport previously
74 attempted to predict wind shear using the WRF model, affirming its capability to
75 forecast wind shear induced by terrain changes several hours in advance and studied
76 the model's performance under non-temperature inversion conditions, it reproduced
77 wind shear characteristics well. However, providing precise warnings for the airport
78 proved challenging(Chan PW.2016).Building on this, Hong Kong International
79 Airport conducted further research: using a 200m resolution numerical weather

80 prediction model, AVM, designed for fine short-term weather forecasting based on
81 WRF3.4.1 and during the whole research period, the results consistent with the
82 model forecast were observed on both runways(Hon K K.2020). Since then, Hong
83 Kong International Airport improved the WRF-based coupled model, utilizing the
84 WRF-LES coupled model to capture many wind characteristics and micro-scale
85 airflow within the airport, accurately reproducing real wind direction changes (Chen
86 F.2022). These studies demonstrate the effectiveness of numerical models in
87 simulating low-level wind shear in airport regions, with higher resolution models
88 providing better simulation results. The series of studies conducted at Hong Kong
89 International Airport suggests that improving models based on the WRF model or
90 coupling it with other models is a promising approach for studying low-level wind
91 shear. In previous studies, the WRF/CALMET coupled model has never been used to
92 study low-level wind shear in airport regions. This study uses this model, significantly
93 improving simulation resolution and leveraging CALMET's advantages in wind field
94 calculations, providing a new method for numerical simulation of low-level wind
95 shear in airport areas.

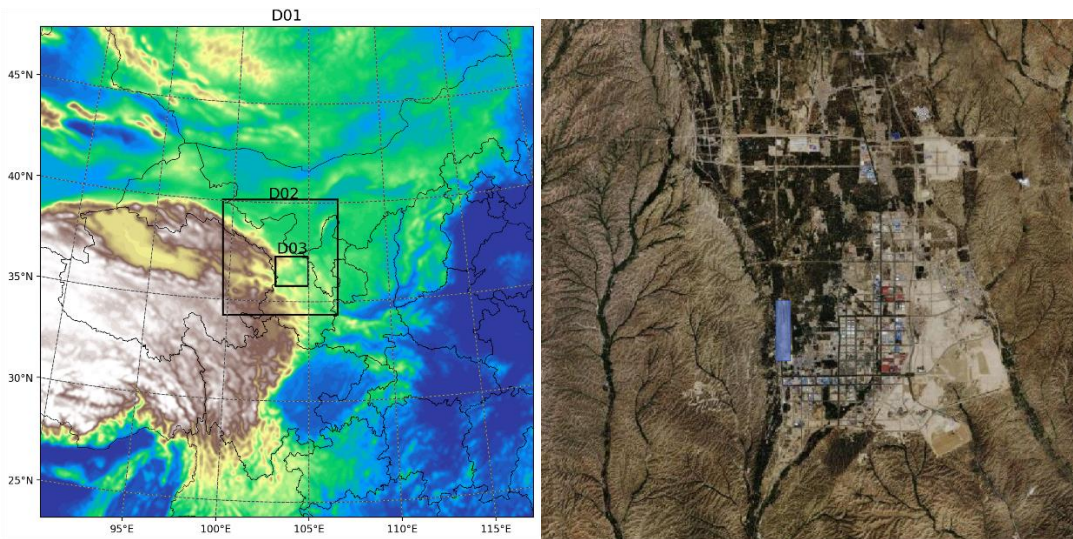
96 Lanzhou Zhongchuan International Airport stands as one of the largest aviation
97 hubs in Northwest China, situated in the southeastern part of the Qinwangchuan
98 alluvial-fan basin, surrounded by mountains on all sides. The region is known for
99 frequent wind shear occurrences, a phenomenon that has become increasingly
100 common at Lanzhou Zhongchuan Airport due to the rapid growth in the number of
101 flights. Most wind shear events occur during spring and summer, particularly in May,
102 June, and July (Li L.2020). Statistical reports on wind shear at Lanzhou Zhongchuan
103 Airport indicate that the majority of incidents occur in the afternoon and evening.
104 This trend is attributed to the downward momentum in the afternoon, enhanced
105 convective activity from increased ground heating, and higher wind speeds. Severe
106 convective weather is more likely to occur in the late afternoon to evening,
107 contributing to a higher frequency of reported low-level wind shear events.
108 Conversely, fewer flights operate during the night, accompanied by reduced
109 convective weather, resulting in relatively fewer reports of aircraft encountering low-
110 level wind shear (Dang B.2013). In May 2016, Zhongchuan Airport installed coherent
111 Doppler lidar near the runway to study the characteristics of low-level wind shear
112 and provide warnings (Li L.2020). Numerical simulation studies on wind shear at
113 Zhongchuan Airport have been ongoing. Jiang L. et al. selected a 6 km×6 km area near
114 the runway at Zhongchuan Airport to establish a digital elevation model of the terrain.
115 They used FLUENT software for numerical simulation, solving iterative calculations
116 to obtain the distribution characteristics of wind speed and pressure in the simulated
117 area (Jiang Lihui.2018). However, FLUENT, being a Computational Fluid Dynamics
118 (CFD) simulation software widely used in engineering, science, and research fields,
119 only considers the local turbulence of terrain and buildings on the flow field. It does
120 not account for factors such as gravity and heat exchange in real atmospheric
121 conditions. Therefore, relying solely on FLUENT for simulating and warning wind
122 shear at Zhongchuan Airport has its limitations. Improvements in simulating low-
123 level wind shear still require enhancements built upon numerical weather
124 forecasting models.

125 In both domestic and international research, the CALMET model is frequently
126 employed to downscale WRF, providing a finer representation of microscale terrain
127 structures. Particularly in weak wind conditions, the CALMET downscaling coupling
128 model outperforms WRF in simulating near-surface wind directions(Zhang D.2020).
129 The WRF/CALMET coupled system demonstrates satisfactory performance in
130 various challenging scenarios, including the complex terrain of the Qinghai-Tibet
131 Plateau(Liao R.2021) and the intense weather system of Super Typhoon Meranti
132 (2016)(Tang S.2021). Up to now, no one has used WRF/CALMET coupling system to
133 simulate and test the occurrence of low-altitude wind shear. Therefore, this study
134 leveraged the dynamic downscaling effect of the CALMET model on local micro-
135 terrain to achieve high-resolution wind shear simulations with relatively low
136 computational requirements within a small area. Additionally, we conducted
137 controlled variable experiments by modifying the original terrain. This approach has
138 not been attempted in studies investigating terrain-induced wind shear at other
139 airports. It provides an improved method for simulating low-level wind shear within
140 the WRF model.

141 **2. Mode, Data, Method and Experimental Setup**

142 2.1 Models and Experimental Setup

143 In this study, the WRF model (version 4.2) was employed to simulate a severe
144 convective weather event occurring in the vicinity of Zhongchuan Airport over a
145 duration of 96 hours, starting from July 2, 2022, at 0000 UTC. The simulated wind
146 field results were then downscaled to 100 meters through coupling with the CALMET
147 model. The model utilized a three-layer, two-way nested domain configuration
148 (Figure 1a), with horizontal grid spacings of 9 km, 3 km, and 1 km. In the vertical
149 direction, there were 39 complete Eta layers from the surface to 0 hPa. The physical
150 schemes employed by WRF are detailed in Table 1.



151

152

(a)

(b)

153 Figure 1. Three-layer Nested Domains of the WRF Model (a) and Simulation Area of
154 the CALMET Model © Google Maps(b), with the Zhongchuan Airport Highlighted in
155 Blue

156 Table 1. Model Configuration

Physical Scheme	WRF Option
Microphysics	Thompson graupel scheme (2-moment scheme in V3.1)
Cumulus parameterization	Tiedtke scheme
Longwave radiation	RRTMG
Shortwave radiation	RRTMG
Surface layer	Monin-Obukhov (Janjic Eta) scheme
Land surface	Noah
Boundary layer	MYJ

157 The diagnostic model utilized in this research is the CALMET model (version 6.5),
158 which constitutes the meteorological component of the California Puff Dispersion
159 Model (Scire J S.2000). In the configuration of this study, the initial guessed wind field
160 is obtained from the grid wind field generated by the innermost domain of WRF, with
161 a horizontal grid spacing of 1 km (D3 in Figure 1(a)). Since no objective analysis
162 procedure is employed, we only pay attention to the first step wind field. The
163 coverage area of the CALMET model encompasses Zhongchuan Airport and its
164 surrounding 38km×38km region (Figure 1(b)), with a horizontal resolution of 100m.
165 The vertical layers are set to 10 height levels within 600 m from the ground (the
166 height range influenced by low-level wind shear).

167 Terrain Sensitivity Experiments for Demonstrating the Impact of Terrain on
168 Wind Shear Simulation in CALMET:

169 (1) CALMET: CALMET model configured with default settings as described earlier.

170 (2) CALEMFT_FLAT: Modification in the TERREL terrain processing module where
171 the elevation of all grid points is adjusted to 2000 meters. This adjustment facilitates
172 CALMET simulation on a flat underlying surface.

173 (3) CALEMFT_RAISE: Modification in the TERREL terrain processing module
174 where the elevation of grid points with an altitude exceeding 2050 meters is
175 increased by 1.5 times. This modification enables CALMET to simulate wind shear
176 over a more rugged terrain.

177 These terrain sensitivity experiments are designed to showcase how variations
178 in terrain impact wind shear simulation within CALMET. The CALMET_FLAT
179 experiment simulates wind shear on a flat surface, while the CALMET_RAISE
180 experiment explores wind shear simulation over steeper terrain. The comparison of
181 results from these experiments with the default CALMET setting will provide insights
182 into the sensitivity of wind shear simulations to terrain variations.

183 2.2 data

184 The terrain data comes from the global 90 m digital elevation data set of Shuttle
185 Radar Topography (SRTM3 V4.1) of NASA, and the land use data comes from the
186 global land cover type data with 10m resolution of Pengcheng Laboratory
187 (<https://data-starcloudpcl.ac.cn/zh>) of Tsinghua University in 2017.

188 The horizontal resolution of the ECMWF Reanalysis v5 (ERA5) dataset is $0.25^\circ \times$
189 0.25° , with a temporal resolution of 1 hour. This dataset is employed as both the initial
190 input and boundary fields for WRF model. Additionally, this study utilizes ERA5
191 variables, specifically geopotential height and temperature, for analyzing weather
192 systems during periods of intense convection.

193 Observational data for ground-level 10m wind speed at Lanzhou Zhongchuan
194 Airport are sourced from historical wind speed records provided by the National
195 Oceanic and Atmospheric Administration (NOAA)
196 (<https://www.ncei.noaa.gov/maps/daily/>) with a temporal resolution of 1 hour. The
197 ground 10m wind speed data of WRF model, CALMET model and ERA5 reanalysis
198 data are interpolated to the location of Zhongchuan Airport, and compared with the
199 observed data to verify the performance of the models.

200 2.3 method

201 To quantify the differences in 10m wind speed among the experiments, the
202 following statistical metrics are employed:

203 Index of agreement (IA):

$$204 IA = 1 - \frac{\sum_{i=1}^N (P_i - O_i)^2}{\sum_{i=1}^N (|P_i - \bar{O}| + |O_i - \bar{O}|)^2} \quad (1)$$

205

206 Root-mean-squared error (RMSE):

$$207 RMSE = \sqrt{\frac{1}{n} \sum_{i=1}^n (O_i - P_i)^2}. \quad (2)$$

208 Mean relative error (MRE):

$$209 MRE = \frac{1}{n} \sum_{i=1}^n \frac{(P_i - O_i)}{O_i} \quad (3)$$

210 Here, \bar{O} and \bar{P} represent the average values of observational and simulated data,
211 respectively. Each observed value is denoted as O_i , and each simulated value is
212 denoted as P_i . Smaller values for MRE and RMSE, and an IA closer to 1.0, indicate
213 better simulation performance.

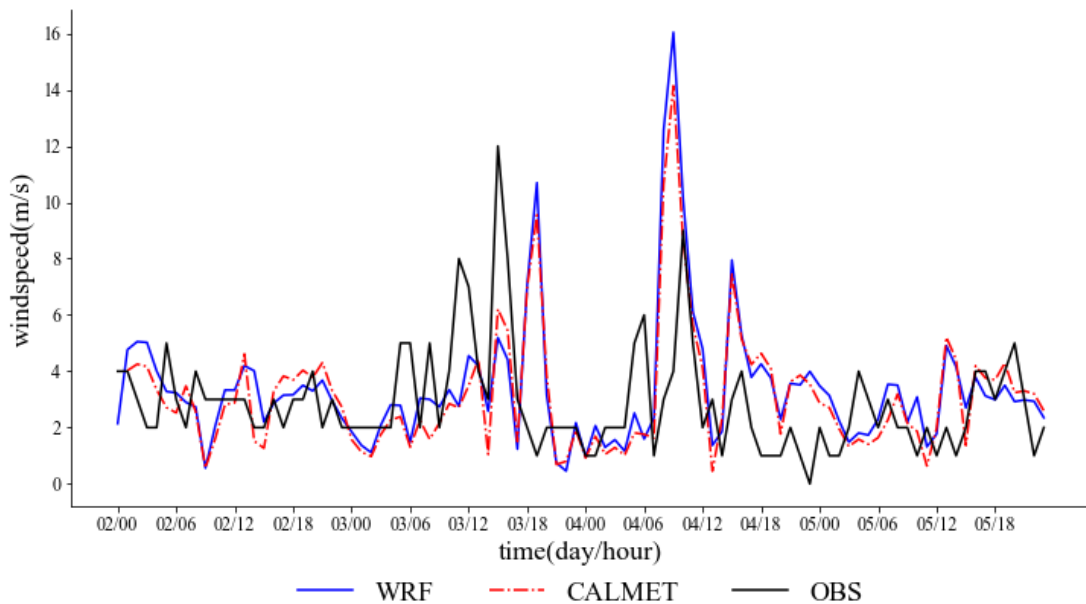
214 Wind shear can be categorized into three types: vertical shear β , meridional
215 horizontal shear α_1 , and zonal horizontal shear α_2 . Among these, vertical shear of
216 horizontal wind has a more significant impact on aircraft takeoff and landing

217 compared to the other types(Bretschneider, L.2022). It results in changes in wind
218 speed and direction as an aircraft moves through different altitudes, which can lead
219 to drastic changes in airflow during ascent or descent, thereby increasing flight
220 difficulty, particularly during takeoff and landing(Keohan, C.2007; Eggers, A.J.,
221 Jr.2003; Eggers, A.J., Jr.1992).

222 **3.Result**

223 3.1 Improvement of WRF/CALMET coupling model for simulation of low-level
224 wind shear.

225 We evaluated the performance of two models in simulating near-surface wind
226 speeds, as shown in Figure 2 and Table 2. Both models showed better agreement with
227 observed data during periods of low wind speeds before convective development
228 (06:00 on July 3) and after convective cessation (02:00 on July 5). During periods of
229 intense convection, both models captured wind speed variability. Although both
230 experiments underestimated or overestimated peak wind speeds on July 3 and July 4,
231 CALMET slightly outperformed WRF in simulating high wind speeds. Furthermore,
232 Table 2 indicates that CALMET's Mean Relative Error and Root Mean Squared Error
233 were lower than those of WRF throughout the entire simulated period, with
234 improvements of 11.13% and 7.24%, respectively. CALMET's Index of Agreement
235 was also closer to 1 compared to the WRF experiment, with an improvement of
236 12.06%. These results demonstrate CALMET's superior overall simulation
237 performance compared to WRF.



238
239 Figure 2 :the time series of 10m surface wind speed for both numerical
240 simulations and observational data

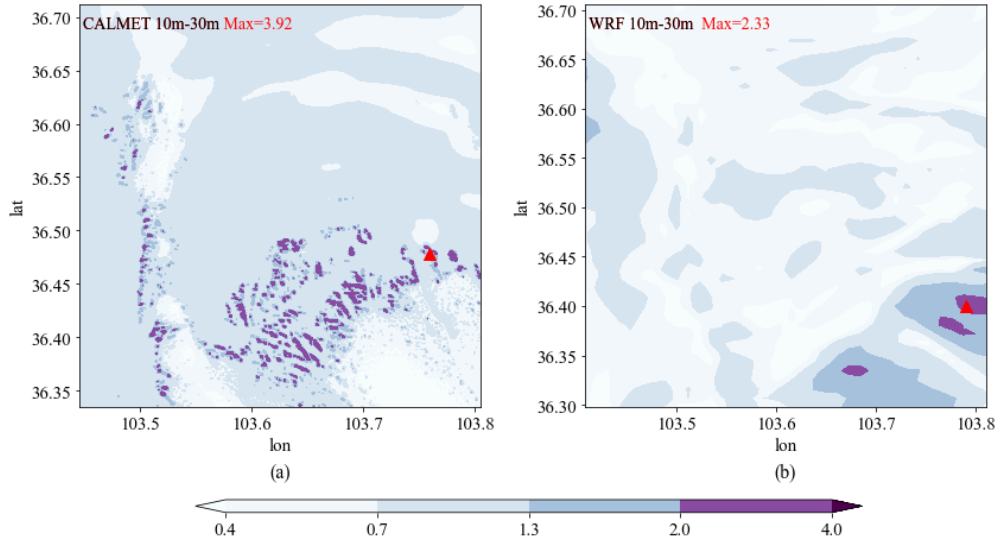
241

242
 243 Table 2: Statistic results of near-surface wind speed simulations in different
 244 experiments averaged.

	WRF	CALMET	Improvement (%)
MRE (%)	43.255	38.425	11.13
RMSE(m /s)	2.713	2.517	7.24
IA	0.454	0.509	12.09

245 At 16:00 on July 3, significant fluctuations in surface wind speeds mark the onset
 246 of convective development (Figure 2). Figure 3 illustrates the distribution of Vertical
 247 Wind Shear (VWS) simulated by both models. In the layer between 10m and 30m
 248 above ground level, CALMET's maximum VWS values, while consistent in location
 249 with WRF's, are notably higher. Terrain analysis reveals CALMET simulates high VWS
 250 values near mountain foothills and western slopes (Figure 8) . WRF's high VWS
 251 values primarily occur in mountainous regions. Details for the height layers of 200m-
 252 300m and 500m-600m can be found in the appendix. Overall, both models exhibit
 253 decreasing VWS with increasing height. From the overall distribution of VWS,
 254 CALMET can simulate a wider range of third and fourth level wind shears, which are
 255 associated with severe and extreme turbulence affecting aircraft takeoff and landing.
 256 Furthermore, this capability provides valuable warnings for aircraft operations at
 257 Nakawa Airport.

258 The atmosphere above and surrounding the mountainous terrain is
 259 characterized by three distinct regions or inclined layers, comprising the thermal
 260 structure undergoing diurnal variations and forming diurnal winds: slope
 261 atmosphere, valley atmosphere, and mountain atmosphere(Zardi, D.2013). It is
 262 challenging to observe any pure form of diurnal mountain wind system, as each
 263 component interacts with the others. Well-organized thermally driven flows can be
 264 identified over a broad spatial scale, ranging from the dimensions of the largest
 265 mountain ranges to the smallest local topography. Therefore, concerning wind shear
 266 in mountainous and foothill areas, wind shear in mountainous areas tends to be
 267 smaller. When airflow passes through mountain ridges, the lower-level airflow
 268 experiences significant compression. According to the conservation of flux, the
 269 acceleration effect on lower-level airflow exceeds that on upper-level airflow,
 270 resulting in an overall reduction in wind shear. When the acceleration effect on lower-
 271 level airflow is significant while the upper-level acceleration effect is weak or absent,
 272 negative wind shear occurs. Overall, the intensity of low-level wind shear may be
 273 greater near mountain foothills or ridges and lesser in valleys or slopes. Hence, the
 274 regions of maximum wind shear simulated by CALMET near mountain foothills or
 275 ridges are more consistent with reality than those by WRF.



276

277 Figure 3: Vertical Wind Shear (VWS) at 16:00 on July 3, 2022, simulated by
 278 CALMET (a) and WRF (b) (Unit: m/s/10m). Triangles indicate the locations of
 279 maximum values.

280 Figure 4 presents the time series of maximum VWS simulated by WRF and
 281 CALMET. It can be observed that both WRF and CALMET simulations exhibit a clear
 282 diurnal pattern in maximum VWS: maximum values are relatively small around dawn
 283 and in the morning (1:00 to 12:00), with minimal fluctuations, while they increase
 284 significantly in the afternoon and evening (13:00 to 24:00), showing larger variations.
 285 However, the maximum values simulated by WRF are generally lower than those by
 286 CALMET, with this difference being more pronounced in the afternoon and evening.
 287 On July 3rd and 4th, during periods of intense convective activity, CALMET is able to
 288 simulate larger fluctuations in maximum VWS compared to normal conditions.

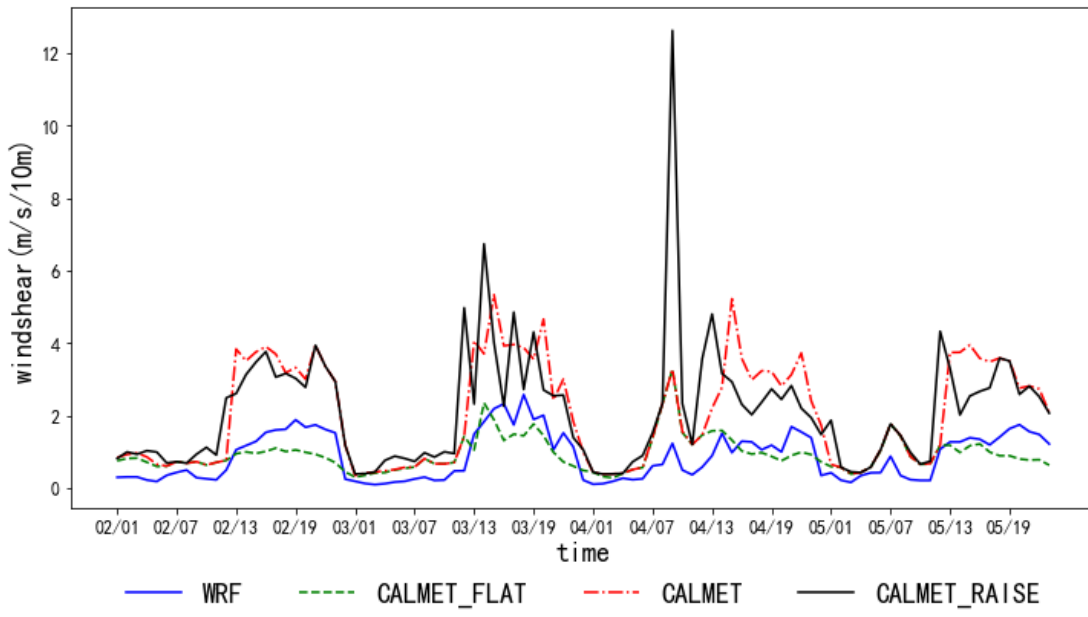
289 In summary, utilizing CALMET for downscaling WRF output of wind fields
 290 provides higher resolution and more precise surface conditions, which are
 291 advantageous for simulating mesoscale wind shear. This is primarily manifested in
 292 the following aspects: the distribution of VWS in the mid-to-low levels is more
 293 significantly influenced by terrain, and VWS decreases more rapidly with increasing
 294 altitude; the diurnal variation of maximum VWS within VWS regions follows a clear
 295 pattern and can reflect the characteristics of intense convection.

296 3.2 Impact of Topography on Wind Shear Simulation

297 Through different terrain configurations, we explored CALMET's detailed terrain
 298 impact on low-level wind shear. We found that valley winds affect VWS diurnal
 299 variation. Terrain, blocking effects, and slope flow kinematics enhance near-surface
 300 airflow diversion, deflection, and ascent over complex terrain, significantly
 301 influencing VWS, with the impact decreasing with height.

302 In the CALMET_FLAT experiment, the increase in maximum VWS during the
 303 afternoon and evening is minimal(Figure 4), with slight fluctuations and values
 304 around 2 m/s/10m, sometimes even lower than WRF. However, good agreement is
 305 observed among the three experiments during the early morning and morning
 306 periods. In CALMET_RAISE, particularly on July 3rd and 4th during intense convective
 307 development, fluctuations in the afternoon and evening are more pronounced
 308 compared to CALMET. However, CALMET_RAISE shows stability similar to CALMET
 309 just before convective development on July 2nd, except for an unusually high value at
 310 09:00 on July 4th, where fluctuations are more pronounced, but numerically close to
 311 CALMET.

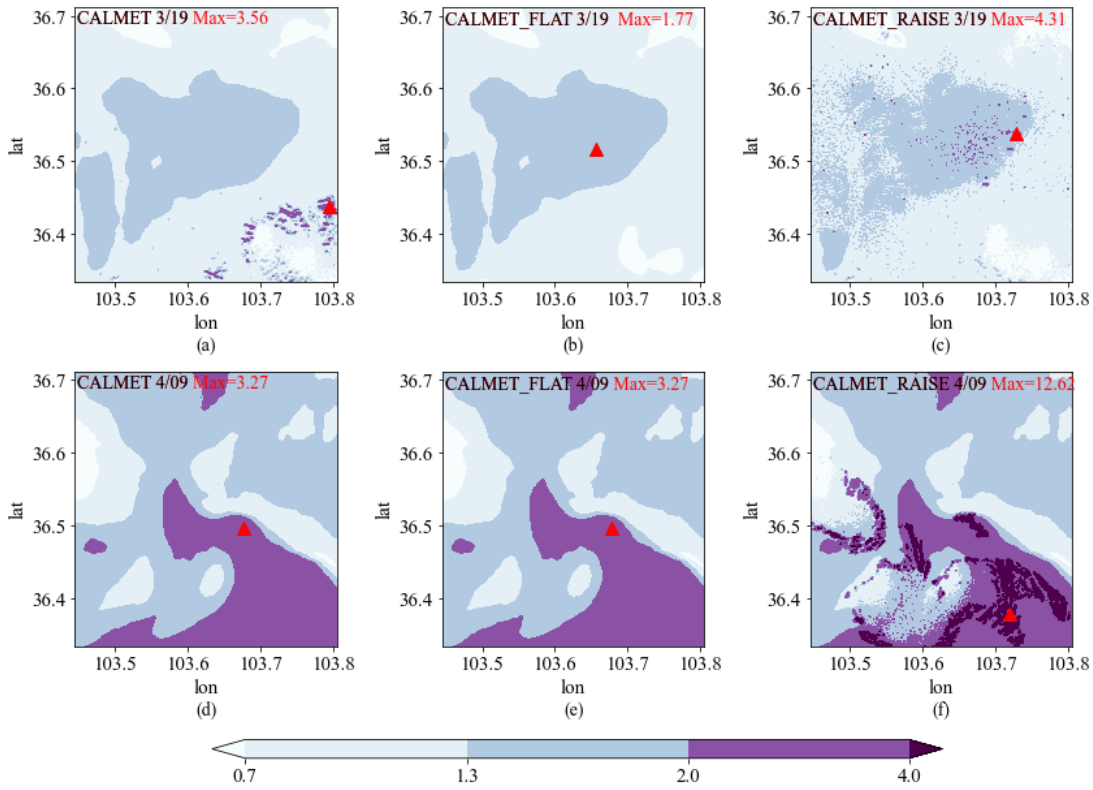
312 In the afternoon and evening, CALMET_FLAT shows a significant decrease in
 313 maximum VWS, while CALEMT_RAISE exhibits more pronounced fluctuations. For
 314 example, at 19:00 on July 3rd (Figure 5(a)-(c)), in the CALMET experiment, the
 315 maximum VWS (3.56 m/s/10m) occurs in the southeastern foothills and valley areas.
 316 In CALMET_FLAT, except for the absence of a high-value area in the southeast, the
 317 distribution is similar to CALMET, with a maximum value of 1.77 m/s/10m in the
 318 central region, which is also a flat valley area in CALMET. In CALMET_RAISE, due to a
 319 sudden 1.5-fold increase in terrain elevation above 2050m, the steep terrain causes
 320 chaotic wind shear distribution, with scattered high values in the central region, and
 321 the maximum value increases to 4.31 m/s/10m. In summary, transitioning from
 322 complex to flat terrain shifts the location of maximum VWS from mountainous areas
 323 to flat valleys.



324

325 Figure 4: Time series of 10m-30m maximum VWS values of different
 326 simulation experiments in the study area

327 This phenomenon is a typical result of valley winds, driven by the interaction
 328 between terrain and solar radiation. During the day, sunlight heats the surface,
 329 leading to differential heating rates between slopes and valleys due to their distinct
 330 topographies. Slopes, receiving direct sunlight, warm up faster than valleys. At night,
 331 the surface loses heat, particularly in valleys with good heat dissipation, resulting in
 332 strong nighttime cooling effects. The temperature difference between slopes and
 333 valleys during the day induces upslope airflow along the slopes. As the heated air
 334 ascends, airflow forms over the valleys, as depicted in Figure 5(a) where maximum
 335 VWS occurs near mountainous areas. At night, cold air flows downhill along the slopes,
 336 forming downslope winds, which reverse the airflow pattern observed during the day.



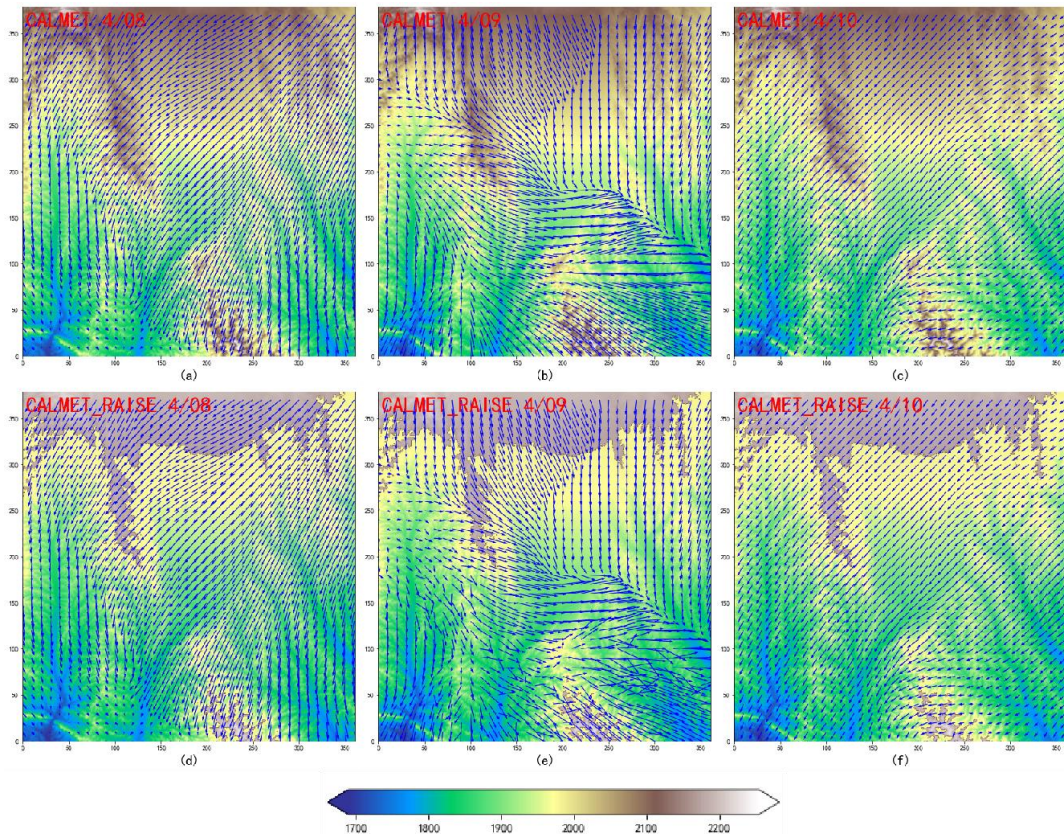
337

338 Figure 5: VWS distribution of 10m-30m.(a)-(c): 19:00 on July 3, 2022; (d)-(f):
 339 09:00 on 4 July 2022; (a),(d):CALMET; (b),(e):CALMET_FLAT;
 340 (c),(f):CALMET_RAISE.

341 The results indicate that CALMET model simulations of VWS are highly sensitive
 342 to terrain: VWS values are generally lower in flat terrain compared to complex terrain,
 343 and the influence of terrain on wind shear diminishes rapidly with height. In
 344 extremely steep terrain, near-surface distribution appears chaotic, but VWS values
 345 notably increase above the surface compared to complex terrain. Across the three
 346 experiments, the absolute differences in VWS decrease with height, suggesting a
 347 diminishing impact of terrain on CALMET model simulations of VWS with increasing
 348 altitude.

349 To investigate extreme high values of VWS in the CALMET_RAISE experiment at
 350 09:00 on July 4th, Figures 5(d)-(f) display the VWS distribution for all experiments at
 351 this time, while Figure 6 presents wind vector maps for three hours for both CALEMNT
 352 and CALEMNT_RAISE. The VWS distribution for CALEMNT and CALEMNT_FLAT is similar,
 353 with a peak of 3.27m/s/10m in the central region. Compared to July 3rd at 19:00,
 354 both experiments show extensive high-value areas in the southeast, with
 355 CALMET_RAISE reaching an exceptional maximum of 12.62m/s/10m in the
 356 southeastern valley area. Additionally, CALMET_RAISE exhibits large areas of
 357 exceptionally high values compared to the other experiments.

358 In Figure 6, at 08:00 and 10:00 on July 4th, the prevailing wind direction in the
 359 area is northeast. Both CALMET and CALEMNT_RAISE show similar wind field
 360 structures, transitioning from northeast to north as terrain slopes southward. When
 361 airflow passes through the southern valley, mountain ranges create denser wind
 362 vectors and increased speeds. However, at 09:00, a strong northwest airflow
 363 converges with the northern airflow, forming a distinct "micro-front." The terrain
 364 blocking induces diversion, deflection, and upward motion of the northwesterly wind,
 365 creating extensive high-value VWS areas in the southeast. Compared to CALMET,
 366 CALEMNT_RAISE exhibits a more chaotic wind field due to increased terrain.



367
 368 Figure 6. Topographic Elevation (unit: m) and Wind Vector Distribution. (a)-(c)
 369 CALMET; (d)-(f) CALMET_RAISE; (a), (d) July 4th, 08:00; (b), (e) July 4th, 09:00; (c),
 370 (f) July 4th, 10:00.

371 In conclusion, the widespread high-value VWS area observed at 09:00 on July 4th
372 resulted from a shift in wind direction to the northwest, encountering minimal
373 velocity reduction before reaching the tall terrain in the south, where the
374 mountainous obstruction led to diversion, deflection, and upward motion. The
375 anomalously high values in the CALEMNT_RAISE experiment were attributed to the
376 elevation of the terrain, significantly intensifying the effects of diversion, deflection,
377 and upward motion. This suggests that terrain has a more pronounced impact on
378 CALMET-simulated wind shear during high wind speeds, while its influence is less
379 evident during low wind speeds. Therefore, heightened awareness of low-level wind
380 shear occurrence is warranted in complex terrain.

381 **4 Conclusion**

382 In order to investigate whether higher-resolution numerical models yield better
383 simulation results for low-level wind shear, this study focuses on a severe convective
384 weather event that occurred in the vicinity of Zhongchuan Airport on July 2, 2022.
385 The WRF/CALEMNT coupled model is utilized to simulate the wind field, and the
386 influence of terrain variations on CALMET-simulated wind shear is explored. The
387 main conclusions are as follows:

388 (1) CALMET improves the simulation of near-surface winds, bringing them
389 closer to observed data than WRF, thereby facilitating more accurate modeling of
390 low-level wind shear.

391 (2) The diurnal variation of VWS shows a distinct pattern. CALMET exhibits
392 higher VWS compared to WRF, especially during the afternoon and evening. During
393 periods of intense convective activity, CALMET captures larger VWS fluctuations,
394 including higher peak values. CALMET's finer terrain features result in a VWS
395 distribution that better aligns with terrain effects, with VWS generally higher near
396 foothill areas compared to mountains, and a more pronounced decrease with altitude.

397 (3) Terrain sensitivity experiments show that during early morning and
398 morning hours, the maximum VWS of the three experiments were similar, occurring
399 in flat regions with minimal terrain influence. However, in the afternoon and evening,
400 CALMET_FLAT shows decreased maximum VWS values, while CALMET_RAISE
401 exhibits drastic fluctuations, with peak values near mountainous areas, indicating
402 significant terrain influence. Moreover, the impact of terrain on CALMET-simulated
403 VWS diminishes with altitude. These findings highlight the substantial influence of
404 terrain on CALMET, particularly during periods of high wind speeds.

405 (4) The occurrence of abnormally high VWS values in the simulations is
406 attributed to strong disturbances caused by tall terrain features: wind direction shifts
407 to northwest winds, encountering minimal reduction in wind speed before
408 encountering the tall terrain in the southern region. CALMET_RAISE elevates the
409 terrain from its original level, enhancing channeling, swirling, and updraft effects.

410 CALMET is a mature dynamic regional downscaling tool, and using other
411 numerical weather prediction models can also achieve the scale of CALMET. We chose

412 to use CALMET for the following reasons: from the perspective of operational
413 considerations, conducting research at the same scale requires lower computational
414 requirements and hardware needs for the CALMET model.

415 The research findings of this study are solely based on a short-term simulation
416 period of weather events in the Zhongchuan Airport area. However, this specific case
417 does not necessarily represent the overall wind shear situation at the airport, as it is
418 just one weather event with significant wind shear. And Obtaining radar wind profiler
419 data for the airport poses certain difficulties, we do not have Doppler lidar equipment
420 available. Direct observation of wind shear is challenging. We have made efforts to
421 obtain reanalysis data and site wind speed observations as much as possible. Due to
422 limited funding in the preliminary stages of our research, we could only start with
423 theoretical studies, and field experiments will be conducted once funding becomes
424 available. Our future work will expand to include longer simulation periods in more
425 airports and regions with complex terrain. This expansion aims to examine and
426 quantify the additional value provided by CALMET in simulating low-level wind shear.

427

428 *Competing Interests.* The corresponding author declares that all authors have no
429 competing interests.

430 **Acknowledgment**

431 This work was supported by the Joint Funds of the National Natural Science
432 Foundation of China (Grant No. U2342205), the Gansu Provincial Association of
433 Science and Technology Innovation Drive Promotion Project (Grant No.
434 GXH20230817-7), and the Key Natural Science Foundation of Gansu Province (Grant
435 No. 23JRRA1030). We extend our sincere appreciation to the funding agencies for
436 their support.

437 Additionally, we would like to express our gratitude to the Supercomputing
438 Center of Lanzhou University for their assistance.

439

440 **References**

441 Boilley A, Mahfouf J F. Wind shear over the Nice Côte d'Azur airport: case studies[J].
442 Natural Hazards and Earth System Sciences, 2013, 13(9): 2223-2238.

443 Bretschneider, L.; Hankers, R.; Schönhals, S.; Heimann, J.-M.; Lampert, A. Wind Shear
444 of Low-Level Jets and Their Influence on Manned and Unmanned Fixed-Wing Aircraft
445 during Landing Approach. *Atmosphere* **2022**, *13*, 35.
446 <https://doi.org/10.3390/atmos13010035>

447 Chan PW, Hon KK (2016b) Observation and numerical simulation of terrain-Induced
448 windshear at the Hong Kong International Airport in a planetary boundary layer

449 without temperature inversions. *Adv Meteorol Artic* ID. <https://doi.org/10.1155/2016/1454513>

450

451 Chen F, Peng H, Chan P, et al. Identification and analysis of terrain-induced low-level
452 windshear at Hong Kong International Airport based on WRF-LES combining
453 method[J]. *Meteorology and Atmospheric Physics*, 2022, 134(4): 60.

454 Colman B, Cook K, Snyder B J. Numerical weather prediction and weather forecasting
455 in complex terrain[M]//Mountain Weather Research and Forecasting: Recent
456 Progress and Current Challenges. Dordrecht: Springer Netherlands, 2012: 655-692.

457 Dang, B., W. Z. Sun, J. Y. Wang, et al., 2013: Analysis of low-altitude wind shear cases
458 at Lanzhou Zhongchuan Airport during 2004–2007. *J. Lanzhou Univ. (Nat. Sci.)*, 49,
459 63–69, doi:10.3969/j.issn.0455-2059.2013.01.012. (in Chinese)

460 Eggers, A.J., Jr.; Digumarthi, R.; Chaney, K. Wind Shear and Turbulence Effects on
461 Rotor Fatigue and Load Control. *J. Sol. Energy Eng.* **2003**, 125, 402–409.

462 Evans J, Turnbull D. Development of an automated windshear detection system using
463 Doppler weather radar[J]. *Proceedings of the IEEE*, 1989, 77(11): 1661-1673.

464 Fujita T T, Caracena F. An analysis of three weather-related aircraft accidents[J].
465 *Bulletin of the American Meteorological Society*, 1977, 58(11): 1164-1181.

466 Hon K K. Predicting low-level wind shear using 200-m-resolution NWP at the Hong
467 Kong International Airport[J]. *Journal of Applied Meteorology and Climatology*, 2020,
468 59(2): 193-206.

469 Jiang Lihui, Liu Xiaoyu, Li Zhen, et al. Study on the influence of terrain and buildings
470 around Lanzhou Zhongchuan Airport on wind field [J]. *Computer and Digital
471 Engineering*, 2018, 46(3): 561-565,626.

472 Keohan, C. Ground-based wind shear detection systems have become vital to safe
473 operations. *ICAO J.* **2007**, 62, 16–19, 33–34.

474 Liao R, Fang X, Liu H, et al. Wind characteristic in the complex underlying terrain as
475 studied with CALMET system[C]//Journal of Physics: Conference Series. IOP
476 Publishing, 2021, 2006(1): 012053.

477 Li Hai, Zhou Meng, Guo Qinghua , Wu Renbiao , Xi Jiangtao. Compressive sensing-
478 based wind speed estimation for low-altitude wind-shear with airborne phased array
479 radar[J], *Multidimensional Systems and Signal Processing*,2016,7:1-14

480 Li L, Shao A, Zhang K, et al. Low-level wind shear characteristics and lidar-based
481 alerting at lanzhou zhongchuan international airport, China[J]. *Journal of
482 Meteorological Research*, 2020, 34(3): 633-645.

483 Roland, J. White Effect of wind shear on airspeed during airplane landing approach. *J.
484 Aircr.* **1992**, 29, 237–242.

485 Scire J S, Robe F R, Fernau M E, et al. A user's guide for the CALMET Meteorological
486 Model[J]. Earth Tech, USA, 2000, 37.

487 Tang S, Huang S, Yu H, et al. Impact of horizontal resolution in CALMET on simulated
488 near-surface wind fields over complex terrain during Super Typhoon Meranti
489 (2016)[J]. Atmospheric Research, 2021, 247: 105223.

490 Zardi, D., Whiteman, C.D. (2013). Diurnal Mountain Wind Systems. In: Chow, F., De
491 Wekker, S., Snyder, B. (eds) Mountain Weather Research and Forecasting. Springer
492 Atmospheric Sciences. Springer, Dordrecht. https://doi.org/10.1007/978-94-007-4098-3_2

494 Zhang D, Chen L, Zhang F, et al. Numerical simulation of near-surface wind during a
495 severe wind event in a complex terrain by multisource data assimilation and dynamic
496 downscaling[J]. Advances in Meteorology, 2020, 2020: 1-14.

497 Zhang Y, Jia M. Low-level wind shear of wind field modeling and simulation[J]. 2022.